

Article type: Full Paper

Direct Observation of Interfacial Mechanical Failure in Thio-Phosphate Solid Electrolytes with *Operando* X-Ray Tomography

*Kenneth E. Madsen, Kimberly L. Bassett, Kim Ta, Brandon A. Sforzo, Katarzyna E. Matusik¹, Alan L. Kastengren, and Andrew A. Gewirth**

Department of Chemistry
University of Illinois at Urbana-Champaign
600 S. Mathews Ave.
Urbana, IL 61801 USA

K. E. Madsen, Dr. K. L. Bassett, K. Ta, Prof. A. A. Gewirth
University of Illinois at Urbana-Champaign, Department of Chemistry, Urbana, IL 61801, USA
Email: agewirth@illinois.edu

Dr. B. A. Sforzo
Argonne National Laboratory, Energy Systems Division, Lemont, IL, 60439, USA

Dr. K. E. Matusik, Dr. A. L. Kastengren
Argonne National Laboratory, X-Ray Science Division, Lemont, IL, 60439, USA

Keywords: (Solid Electrolyte, X-Ray Tomography, Mechanical Failure, LGPS, Solvate)

¹ Current affiliation Sigray, Inc.

* author to whom correspondence should be addressed: email: agewirth@illinois.edu; tel: +1217-333-8329

Abstract

Herein we investigate the mechanical behaviors of $\text{Li}_{10}\text{GeP}_2\text{S}_{12}$ (LGPS) solid electrolytes during electrochemical cycling using *operando* x-ray tomography. We demonstrate that the bulk mechanical decomposition of LGPS when cycled against lithium is a direct result of electrochemical reduction of the solid electrolyte at the LGPS/ Li^0 interface. The reductive decomposition of LGPS during lithium plating results in the formation of low-density domains at the electrode/electrolyte interface, which impose sufficient mechanical stress on the underlying LGPS to crack the SE pellet. The critical stress developed prior to pellet fracture is significantly lower than the bulk shear modulus of LGPS, suggesting that the electrochemical instability of LGPS dramatically worsens the mechanical stability of the material near the LGPS/ Li^0 interface. We also show that the application of a highly concentrated liquid electrolyte to the LGPS surface suppresses the reductive decomposition of LGPS, improving both the electrochemical performance and mechanical stability of the bulk LGPS solid electrolyte.

1. Introduction

Since their commercialization in 1991 by the SONY corporation, lithium-ion batteries (LIBs) have become the energy storage medium of choice for small-scale applications due to their high energy and power densities relative to other battery chemistries.^[1] Despite the successful implementation of LIBs in portable electronics, proliferation of Li^+ -based energy storage at larger scales (electric vehicle or grid-scale energy storage) has been hampered by insufficient energy densities, prohibitive material costs, and safety concerns.^[2] While significant progress has been made in the development of high energy density battery materials, the implementation of these materials in practical systems without sacrificing cell longevity or safety remains a pressing scientific challenge.

One of the best studied approaches to improve the energy density of LIBs is to replace existing graphitic anodes (372 mA h g^{-1} capacity) with metallic lithium (3860 mA h g^{-1} capacity).^[3] Unfortunately, uneven lithium plating and stripping in conventional organic liquid electrolytes promotes the growth of lithium dendrites, accelerating the formation of internal short circuits. Additionally, the low thermal stability of electrolyte solvents (often mixtures of cyclic and linear carbonates) incurs exothermic decomposition of the electrolyte in the event of cell failure, often resulting in catastrophic thermal runaway.^[4-6] While many approaches have been explored to address these issues, one of the most promising options is the elimination of the liquid electrolyte in favor of a solid electrolyte.^[7]

Transitioning from conventional liquid electrolytes to Li^+ -conducting solid electrolytes (SEs) presents two primary advantages. The high mechanical rigidity of inorganic SEs may act to suppress the formation of dendrites at lithium anodes, reducing the possibility of internal short circuits.^[8] Additionally, the negligible flammability of most SEs dramatically lowers the risk of uncontrolled thermal runaway in the event of cell failure.^[9, 10] These potential benefits motivate the search for materials with sufficiently high ionic conductivities to serve as replacements for their liquid counterparts. Among the known SE formulations, the thiophosphate class of superionic conductors exhibit exceptionally fast lithium transport at room temperature.^[11] Specifically, $\text{Li}_{10}\text{GeP}_2\text{S}_{12}$ (LGPS) demonstrates an ionic conductivity of ca. 10 mS cm^{-1} , comparable to conductivities achievable in conventional liquid electrolytes.^[12]

Despite the favorable ionic conductivity of LGPS, its poor chemical and electrochemical stabilities remain key challenges for practical application. The narrow window of electrochemical stability of LGPS and many other thiophosphate SEs results in decomposition of the SE at both the anode and cathode surfaces.^[13-18] While progress has been made in the implementation of low voltage cathodes, the reductive instability of LGPS at lithium anodes remains a considerable

issue. Previous investigations of the LGPS/Li⁰ interface have identified Li₂S, Li₃P, Li-Ge alloys, and other P-S and S-S containing species as some of the most common reductive decomposition products formed during lithium plating.^[19, 20] In general these species are poor ionic conductors, and their buildup at the interface results in a progressive decrease in overall ionic conductivity. Likewise, the formation of electronically conductive alloys of Ge allows the reductive decomposition of the SE to propagate into bulk LGPS, precluding the stable passivation of the interface.

In addition to their (electro)chemical instabilities, mechanical instabilities in SEs have also been reported. Recent analyses of garnet and thiophosphate SEs with *operando* x-ray tomography have demonstrated crack propagation through bulk SE pellets during electrochemical cycling. While the mechanisms of crack formation are material-dependent, they have generally been attributed to either lithium dendrite propagation through voids and defects in the SE or to volumetric changes at the electrode/electrolyte interphase due to the electrochemical decomposition of the electrolyte.^[21-24] Regardless of the mechanism, the progressive mechanical failure of SE pellets with cycling results in a sharp decrease in ionic conductivity and allows the facile growth of lithium dendrites through the crack network resulting in subsequent cell shorting.^[8]

One approach to address the (electro)chemical instabilities of SEs is the application of a coating or interlayer to the SE surface, thereby protecting the electrolyte from the extreme potentials of the electrodes.^[16, 25] While both organic and inorganic coatings have been investigated, the application of inorganic coatings often leads to the formation of insufficiently conductive interfacial domains, limiting the practicality of these coatings in a real system.^[26] In contrast, the application of polymeric or liquid interlayers has proven quite effective at mitigating electrochemical decomposition while maintaining fast ion transport.^[27-29] Indeed, previous work

from our group has demonstrated the improved electrochemical stability of thiophosphate solid electrolytes upon modification of the $\text{Li}^0/\text{electrolyte}$ interface with a highly concentrated (solvate) liquid electrolyte.^[30]

The enhanced electrochemical stability resulting from the application of a solvate interlayer has been largely attributed to thermodynamic factors, specifically the suppression of reductive decomposition at the SE/Li^0 interface. While this offers insights into the electrochemical stability of the modified interface, the impact of interlayer modification on the mechanical stability of the SE remains unclear. Much progress has been made in the development of *operando* real-space imaging techniques to study such processes in battery materials under electrochemical load.^[31] In the present work we employ *operando* x-ray tomography to interrogate the mechanical responses of both interlayer-modified and unmodified LGPS solid electrolyte pellets during electrochemical cycling. Leveraging the spatial resolution of the technique we directly image the growth of interfacial decomposition domains responsible for the eventual fracture of the bulk LGPS pellet. We then demonstrate that by the application of a liquid interlayer the formation of these domains can be suppressed, thereby improving both the electrochemical performance and mechanical stability of the solid electrolyte.

2. Results and Discussion

2.1 Electrochemical Performance of Interlayer-Modified and All-Solid-State LGPS Cells

Operando electrochemical measurements were conducted on cold-pressed LGPS pellets (ca. 150 μm thick, 2mm in diameter), cycled voltammetrically in lithium-lithium symmetric cells. Cells without interlayer modification, herein referred to as all-solid-state cells, were assembled by placing the LGPS pellet between two pristine lithium electrodes, creating direct contact between the SE and the Li^0 surface. For cells assembled with an interlayer, herein referred to as interlayer

cells, interface modification was accomplished by painting the surfaces of both lithium electrodes with solvate electrolyte before contacting the LGPS pellet. The solvate, identified in previous investigations to exhibit favorable interactions with LGPS,^[30] consisted of a 6.6 molal solution of lithium bis(trifluoromethanesulfonyl) imide (LiTFSI) in 1,3-dioxolane (DOL)/1,2-dimethoxyethane (DME)/ 1,1,2,2-tetrafluoroethyl 2,2,3,3-tetrafluoropropyl ether (TTE).^[30]

Figure 1a presents voltammetry obtained from *operando* LGPS cells in both the all-solid-state (black) and interlayer (red) configurations, cycled between ± 500 mV at a scan rate of $200 \mu\text{V s}^{-1}$. After several cycles, both cells demonstrate a roughly linear correlation between applied potential and current, reflecting the ohmic behavior expected from a high ionic-conductivity solid electrolyte.^[32] Interestingly, at early cycles (cycles 1-3) the all-solid-state cell deviates from this behavior, exhibiting hysteresis characteristic of diffusion limitations at the electrode/electrolyte interface.^[33] Previous investigations of similar systems attribute the observed diffusion limitations to local Li^+ depletion at the interface, and are indicative of insufficient ion transport to maintain the Li^+ flux demanded by the potential.^[19, 32] Significantly, the lack of a diffusion limitation in the interlayer cell suggests improved Li^+ mobility across the interface relative to the purely solid boundary.

In addition to the differences in interfacial ion depletion, the two cell configurations exhibit different long-term stabilities with cycling. The all-solid-state cell demonstrates a progressive drop in peak current density and concomitant increase in total cell resistance (calculated as the slope of a linear regression applied to each potential sweep) with cycle number, as depicted in Figure 1b. This increased resistance is attributed to reductive decomposition of LGPS at the electrode/electrolyte interface due to the generally poor thermodynamic stability of thiophosphates against metallic lithium.^[14, 15, 34, 35] Notably, the interlayer cell does not display this fade, exhibiting a slowly decreasing cell resistance around $70 \text{ k}\Omega$, nearly half the $120 \text{ k}\Omega$

reached in the all-solid-state cell after 5 cycles. This observation demonstrates the enhanced reductive stability of the modified interface, aligning well with previous reports on both interlayer-modified, and quasi-solid-state electrolytes.^[30, 36, 37]

The origins of the beneficial electrochemical properties of LGPS attendant interlayer modification have been investigated in a previous report from our group where it was found that the presence of the solvate electrolyte impacts both the interfacial and bulk properties of the LGPS pellet.^[30] Specifically, the presence of a highly concentrated liquid electrolyte at the interface serves to both effectively drop the highly reducing potentials induced during lithium plating and to homogenize Li^+ transport between the electrode and the LGPS pellet, thereby enhancing peak current stability. Additionally, the observed decrease in overall cell resistance for the interlayer modified cell has been attributed to the slow permeation of the liquid electrolyte into the LGPS pellet, gradually decreasing grain boundary impedance within the SE and facilitating faster ion conduction across the bulk electrolyte pellet.

In both *operando* cells, sharp current spikes are observed in the later cycles indicative of lithium dendrimers bridging the solid electrolyte pellet resulting in “soft” internal short circuits. In these cases, the sharp jump in current is enough to decompose the dendrimer and return the cell to approximately normal function.^[38, 39] Cells were cycled until failure (an example of which is provided in the SI, Figure S3) wherein an irreparable cell short occurred, typified by a permanent jump in cell current. Generally, the interlayer modified cells exhibit enhanced lifetimes relative to the all solid-state cells, suggesting moderate suppression of lithium dendrite propagation.^[30] One other electrochemical response of note is the presence of periodic current oscillations in all *operando* cells. These oscillations have the same periodicity as tomographic imaging (500 s) and are attributed to photoelectron emission resulting from beam interactions with the electrochemical cell. Notably, the peak current densities, and the rates of peak current

fade elicited by *operando* cells show good agreement with ex-situ cells (Figure S4) suggesting that any putative radiation damage as a result of the x-ray beam is likely negligible.

2.2 Bulk Mechanical Decomposition of All-Solid-State and Interlayer-Modified Cells

Structural changes to bulk LGPS pellets were visualized using cross-sectional reconstructions of tomographic data as a way to monitor the mechanical stability of the SE.

Figure 2a and **b** presents cross-sectional slices from the centers of an all-solid-state and interlayer cell, respectively, along with corresponding electrochemical data. Pixel intensities in the grey-scale images reflect total x-ray attenuation with bright pixels signifying regions of higher total attenuation (LGPS) and dim pixels signifying regions of lower total attenuation (empty space or metallic lithium), scale bars are 1 mm. In most greyscale images, concentric rings of slightly different pixel intensity are found about the center of rotation of the electrochemical cell; these represent reconstruction ring artifacts, as discussed in further detail in the SI (Figure S5). As the change in pixel intensity due to ring artifacts is generally small, and the subsequent analyses rely primarily on global averaging, the impact of these artifacts is expected to be minimal.

Mechanical decomposition is obvious in both cells, as evidenced by crack formation through the LGPS pellets during cycling. The extent of this decomposition is greatest when cycling within a wide potential window (± 0.5 V), with fewer significant mechanical changes observed during narrow window cycling (± 0.1 V) or during open circuit potential holds. In addition to crack propagation, large scale movement of material is seen in the all-solid-state cell, as demonstrated by a piece of material tilting out of the image frame in the upper right-hand corner at later cycling times. Despite the observed mechanical decomposition in both cells, several differences are evident when comparing the mechanical responses of the two configurations.

Visually, the most obvious of these differences is the continuity of the LGPS pellet during cycling. The all-solid-state cell demonstrates substantial pulverization of the SE, similar to other investigations of ceramic solid electrolytes,^[21, 23] whereas the interlayer cell maintains larger continuous domains of LGPS. Furthermore, the rate of crack formation in the all-solid-state cell appears much greater than that of the interlayer cell. Indeed, while the all-solid-state cell appears profoundly fractured after 6.8 h, the interlayer cell never reaches the same extent of structural decomposition, even after 12.8 h of continuous cycling.

To better quantify these observations, the total void volume was computed along with the internal surface area of the crack network for both the all-solid-state and interlayer cells, as described in the SI (Figure S6). The results of this analysis for the all-solid-state and interlayer cells are presented in **Figure 3a** and **b**, respectively. In this interpretation, the void volume reflects bulk structural decomposition, while the void surface area quantifies the continuity of the pellet, as reported in previous analyses of fatigue driven mechanical failure.^[40-42] For both cells void volume and void surface area increase monotonically with cycling, reflecting the irreversible mechanical decomposition of the pellet. The enhanced mechanical stability afforded by the solvate is evident, as the interlayer cell demonstrates substantially lower void volume and surface area even after nearly twice the cycling time.

To better understand the mode of mechanical failure, derivative traces of void volume with respect to time for the all-solid-state and interlayer cells were computed and are presented in Figure 3c and d, respectively. In the all-solid-state cell, a clear correlation exists between the rate of void formation and the cell potential, suggesting that, either the passage of current, or the polarization of the electrode to extreme potentials results in mechanical decomposition of the LGPS pellet. In contrast, the overall rate of void formation is lower in the interlayer cell, and the correlation between void formation and cell potential is much less apparent. This suggests that the

presence of the solvate interlayer both reduces the rate at which void space forms and works to decouple the mechanical decomposition of the SE from electrochemical processes.

2.3 Interfacial Properties of All-Solid-State LGPS Cells

The results displayed in Figure 3 demonstrate that modifying the LGPS/Li⁰ interface by the addition of a solvate interlayer strongly impacts the mechanical evolution of the solid-electrolyte pellet. To further understand the origins of this effect, three-dimensional renderings were computed for both the all-solid-state cell and the interlayer cell, using grayscale pixel intensities to segment volume data. These renderings directly capture the interfacial structure of the LGPS pellet as cycling progresses. **Figure 4** shows a time-dependent sequence of these renderings for the all-solid-state cell along with the corresponding electrochemical data. For each time point a full three-dimensional reconstruction of the SE pellet is depicted in real space with the height of each point along the pellet reflected by the color map (the top of the pellet is depicted in yellow and the bottom of the pellet is depicted in blue). The figure shows a prominent morphological change at the LGPS/Li⁰ interface through the formation of topologically heterogeneous regions (depicted here as bright yellow domains) protruding vertically from the SE surface. These regions likely result from inhomogeneous contact between the SE and the Li surface. Indeed, heterogeneous contact between Li and other SE materials has long been an issue.^[43, 44] The formation of these protrusions appears to be irreversible, supporting the conclusion that the species formed at the interface are the result of electrochemical decomposition of the solid electrolyte. Further, the large size of the domains formed suggests that the decomposition reaction grows from the interface into the bulk, likely due to the formation of electronically conductive Li_{3.75}Ge as one of the primary decomposition products. Electronic conductivity through the decomposed domains allows the reductive decomposition to continue even when the domain size is large.

Additional characterization of the decomposition species for the all-solid-state cell is presented in **Figure 5**, which shows tomographic slices at the end of cell cycling ($t \approx 6.8$ h) taken from positions near the LGPS/Li⁰ interface (Figure 5a) and at the center of the SE pellet (Figure 5b). There is a substantial difference in the pixel intensity distributions near the interface compared with those of the bulk pellet. Large domains of material with intermediate pixel intensity (between that of void space and bulk LGPS) are found near the interface which are absent in the center of the pellet. To quantify this phenomena, histograms of pixel intensities were computed in the areas demarcated by red circles in Figure 5a and b, the results of which are presented in Figure 5c. At the center of the pellet, pixel intensities largely fall within a bimodal distribution, with pixels binned either as void space/Li⁰ or bulk LGPS. A third population of intermediate pixel intensity is observed at the interface signifying the presence of a new material phase that cannot be attributed to either bulk LGPS or void space/metallic lithium.

The approximate composition of the domains formed near the LGPS/Li⁰ interface was estimated by comparing the pixel intensities of these domains to the intensities expected of the common decomposition products of LGPS. Previous work has demonstrated that the primary species formed during the reduction of LGPS are Li₂S, Li₃P, and Li_{3.75}Ge in molar ratios dictated by the stoichiometry of LGPS.^[11, 19, 20] As these species cannot be isolated directly from grayscale images, their expected pixel intensities were estimated based on their total x-ray attenuation coefficients (μ , cm⁻¹). Attenuation coefficients were calculated for each component as the product of its density (ρ , g cm⁻³) and its x-ray mass attenuation coefficient (μ/ρ , cm² g⁻¹) and normalized by the total attenuation coefficient of the LGPS pellet. The theoretical pixel intensity for each component was then calculated as the product of the pixel intensity of the LGPS pellet and the normalized attenuation coefficient. Mass attenuation coefficients for each species were obtained from the NIST photon cross-section database,^[45] and material densities were obtained from

previous literature with the exception of the LGPS pellet whose density was determined experimentally.

Table 1 presents the results of the above analysis, as well as all parameters used to estimate the pixel intensities of the species under investigation. Of the decomposition products considered here, both Li_2S and Li_3P are expected to exhibit lower pixel intensities than LGPS as a result of their low mass attenuation coefficients. In contrast, the mass attenuation coefficient, and therefore the expected pixel intensity, of $\text{Li}_{3.75}\text{Ge}$ is substantially greater than that of LGPS due to the large electron density of Ge relative to P and S. While Li_2S and Li_3P agree qualitatively with the low pixel intensities observed experimentally, their calculated intensities are too low for a confident assignment. Similarly, the high calculated pixel intensity of $\text{Li}_{3.75}\text{Ge}$ disagrees qualitatively with experiment, suggesting that the decomposition domains at the interface cannot be attributed to a single decomposition product.

As no single species can be assigned to the observed decomposition domains, a mixed phase of the three species is considered. The composition of this phase was treated as $12 \text{Li}_2\text{S} + 2 \text{Li}_3\text{P} + \text{Li}_{3.75}\text{Ge}$ as reported elsewhere for the reduction of LGPS against lithium.^[20] The absolute pixel intensity of this phase was treated as an average of the pixel intensities of each species weighted by their molar ratios within the phase. The calculated intensity from this approximation ($4.4 \pm 0.5 \times 10^{-4}$) agrees closely with the experimental pixel intensity of the decomposition domains ($4.5 \pm 1.0 \times 10^{-4}$) supporting the conclusion that the decomposition products observed near the interface are comprised, primarily, of Li_2S as well as small amounts of Li_3P and $\text{Li}_{3.75}\text{Ge}$. While this approximation cannot, unambiguously, assign the composition of the interfacial species, the results are in good agreement with the previously reported composition expected from the stoichiometric reduction of LGPS into its common decomposition products.

To quantitatively monitor the formation of these decomposition products at the LGPS/Li⁰ interface as a function of electrochemical cycling, the total volume of decomposed species was computed by deconvolution of the pixel intensity distributions as a linear sum of three Gaussian populations (details of this analysis are presented in the SI, Figure S7). The results of this volume analysis are presented in **Figure 6a**, which shows that the volume of decomposed material increases on both sides of the LGPS pellet as cycling progresses. In the absence of a true working or counter electrode in the symmetric cell geometry, electrodes are referred to herein by their physical position relative to the LGPS pellet. In all measurements the “Top” electrode (red traces) was subjected to reductive polarization first, followed by the bottom electrode (blue traces). Derivative traces of the data presented in Figure 6a are provided in Figure 6b, where a clear correlation exists between the potential of the electrode and the rate of surface decomposition at the LGPS/Li⁰ interface. Specifically, upon reductive polarization of the top electrode LGPS decomposes readily, in good agreement with previous work in our group suggesting that LGPS decomposes at potentials below 0.1 V vs. Li⁺⁰.^[19] Further, upon oxidative polarization of the top electrode, decomposition on the bottom electrode is evident as this electrode becomes reducing towards LGPS.

To understand the consequences of reductive decomposition, individual decomposition sites were investigated as a function of electrochemical cycling. **Figure 7** presents a series of 3D renderings of an individual decomposition site at different time points during a single reductive sweep. These renderings were obtained from the top surface of the pellet shown in Figure 4 focusing on the formation of a single protrusion. Again, the color depicts the height of each point along the pellet surface with blue denoting the native surface and yellow representing vertical protrusions from it. As the cell is polarized negatively the decomposed inclusion grows outward across the surface, forming a roughly hemispherical protrusion from the LGPS pellet. Eventually

(after ca. 1.4 h), the inclusion reaches a critical size (ca. 150 μm in diameter), resulting in crack formation at the locus of the nucleation site. After formation, the resultant crack propagates through the entire thickness of the pellet at rates faster than the time resolution of the experiment. Direct comparison between cross-sectional images and surface maps reveals that the origin of nearly all cracks in the material overlap with such a nucleation site at one of the electrodes (Figure S8). Notably we do not observe dendritic lithium growth through these decomposition domains which would appear as void space inside the domains themselves. Similarly, as lithium dendrites found in other solid and liquid electrolytes typically exhibit diameters between 1 and 100 μm they should be visible within the spatial resolution of this technique.^[8, 24, 50]

We next quantify the stresses incurred by the SE at the LGPS/Li⁰ interface. An approximate critical stress was calculated using the average size of the inclusions formed during cycling. The shape of these inclusions was determined from both contrast imaging and orthographic projections of the SE pellet (Figures S7 and S10, respectively) and can be approximated by an oblate spheroid with lateral radii of ca. 72 μm and heights of ca. 19 μm . From this approximate shape a critical stress value was calculated using the bulk elastic modulus of LGPS pellets as reported elsewhere.^[51] The results of this analysis (a detailed description of which is given in the SI, Figure S11) are presented in **Table 2** and reveal a critical stress of ca. 0.8 GPa. This calculated critical stress is substantially lower than the shear modulus reported for cold-pressed LGPS pellets (4.5 GPa)^[52] and an order of magnitude lower than the proposed shear modulus necessary to suppress lithium dendrite formation.^[53, 54] While the mechanical properties of SE pellets are strongly impacted by experimental factors such as synthesis temperature, grain size and pelletizing pressure,^[55] such a large discrepancy between the predicted shear modulus and the apparent measured critical stress must reflect a substantial mechanical instability resulting from the electrochemical decomposition of LGPS in the all-solid-state configuration.

2.4 Interfacial Properties of Interlayer-Modified LGPS Cells

To understand the impact a solvate interlayer has on the LGPS/Li⁰ interface, 3D renderings of the interlayer cell were computed and are presented in **Figure 8**. Several differences are apparent when comparing the renderings obtained from the interlayer cell with those of the all-solid-state cell. One of the most obvious is that, in contrast to the all-solid-state cell, some of the empty volume within the interlayer cell contains liquid electrolyte, which can be directly imaged in the reconstructions due to x-ray attenuation by LiTFSI. 3D renderings show that excess electrolyte (electrolyte which is not pressed between the LGPS and the electrode) forms a corona around the LGPS pellet, pooling (likely due to gravity) at the bottom of the cell. Importantly, as this liquid electrolyte does not extend across the entirety of the cell volume it is not expected to contribute to ionic conductivity during cell cycling.

The mechanical behavior of the interlayer-modified interface strongly contrasts the behaviors exhibited by the all-solid-state interface. As the cell is cycled, the LGPS/Li⁰ interfaces in the interlayer cell remain smooth and nearly constant in appearance, showing no signs of the obvious morphological changes found in the all-solid-state cell. Notably, while cracks form in the pellet with cycling, they cannot be directly tied to interfacial evolution, as they were in the all-solid-state cell. To further confirm this observation, a histogram analysis of pixel distributions near the interface was performed and is presented in the SI (Figure S12). Interestingly, pixel intensities attributable to decomposition products are completely absent from the interface, suggesting that the reduction of LGPS is suppressed by the solvate interlayer.

The contrast between the two cell configurations reported here clearly demonstrates the impact of interfacial processes on the mechanical stability of the SE. In the absence of any interfacial modification, LGPS is subjected to untenably reducing potentials due to its direct contact with the Li⁰ surface. These highly reducing potentials result in the nucleation of

decomposition domains at the LGPS/Li⁰ interface, the appearance of which coincides with the onset of mechanical pulverization. Interestingly, there is no evidence that lithium dendrite growth plays a role in the local mechanical decomposition of the SE pellet. Upon the application of an interlayer to the electrode/electrolyte interface the behavior of the LGPS pellet is markedly different.

The application of a solvate interlayer addresses the thermodynamic instabilities of the SE, which would otherwise result in the interfacial decomposition of LGPS. The highly concentrated electrolyte serves to screen the reducing potentials at the electrode interface, thereby mitigating the reductive decomposition of the LGPS pellet. The absence of interfacial decomposition, and consequently the absence of large decomposition domains, results in lower interfacial stresses which would otherwise result in crack formation across the SE pellet, thereby engendering greatly enhanced mechanical stability to the interlayer-modified electrolyte. Additionally, the interlayer provides the simultaneous advantage of homogenizing lithium transport across the interface, suppressing the formation of highly localized nucleation sites for material decomposition. This combination of homogeneous lithium transport and enhanced thermodynamic stability afforded by the solvated interlayer is thus the origin of the enhanced mechanical stability and electrochemical performance of solvate modified LGPS pellets.

It is worth noting that despite the absence of discernable decomposition at the interface, crack formation is still present in the interlayer cell, albeit to a lesser extent than in the all-solid-state cell. As quantified in Figure 3b, crack formation in the interlayer cell is largely decoupled from the cell potential with the exception of the first cycle within the widened voltage window. This suggests that while the application of the interlayer is effective at mitigating interface driven stress, other stresses within the cell volume still contribute to some mechanical instability in the electrolyte. While the origin of these stresses cannot be determined unambiguously from

tomographic reconstructions, it is likely that they arise from nonuniformities in stack pressure developed during cycling, potentially as a result of macroscopic lithium movement and redistribution at the electrode as has been suggested for both liquid, and solid-polymer electrolytes when employing metallic lithium anodes.^[56-58]

3. Conclusion

Herein the mechanical responses of both unmodified and interlayer modified $\text{Li}_{10}\text{GeP}_2\text{S}_{12}$ solid electrolytes were investigated during electrochemical cycling using *operando* x-ray tomography. We demonstrate that, in the case of the all-solid-state configuration, the electrochemical reduction of LGPS at the Li^0 electrode does not effectively passivate the interface, allowing the decomposition of LGPS to proceed unhindered during lithium plating resulting in the formation of the large decomposed domains at the electrolyte surface. The low density of these domains relative to LGPS imparts compressive stress on the LGPS substrate, apparently independent of the growth of lithium dendrites from the electrode. As the decomposed domain size approaches a critical dimension (ca. 150 μm in diameter) the imposed stress on the substrate exceeds the strength of the pellet forcing the formation of cracks across the bulk SE. The close spatial correlation between decomposition sites and material fracture points suggests that the formation of cracks in the bulk electrolyte is a direct result of stresses imposed by electrochemical decomposition at the LGPS/ Li^0 interface. Further, using the dimensions of these domains, we show that the critical shear stress necessary to fracture the LGPS pellet is 0.8 ± 0.2 GPa, roughly an order of magnitude lower than the proposed shear modulus necessary to prevent lithium dendrite formation. This suggests that electrochemical instabilities at the Li^0 /LGPS interface dramatically reduce the mechanical stability of the SE and, consequently, its ability to prevent lithium dendrite formation during cycling.

In stark contrast to the interfacial changes observed in the all-solid-state cell, the interfaces formed in the interlayer cell exhibit enhanced uniformity during lithium plating and stripping. Specifically, there is no evidence that the decomposition domains found in the all-solid-state cell form at the LGPS/Li⁰ interface when an interlayer is present. This reflects a suppression of the reductive decomposition of LGPS at the interface, in good agreement with previous results from our group demonstrating the thermodynamic stability afforded by the application of the interlayer.^[30] The absence of decomposition domains results in a substantial decrease in interfacial stress during cycling, thereby affording the observed improvements to the bulk mechanical stability of the LGPS pellet. Additionally, the mechanical pliability of the liquid interlayer homogenizes ion transport at the interface, suppressing the formation of inhomogeneous current densities, which are known to lead to additional mechanical instabilities. Thus, while crack formation in the material is evident, the bulk continuity of the pellet is greatly enhanced relative to the all-solid-state cell, likely improving the electrolyte's ability to suppress dendrite propagation. The consequences of this added stability are born out in the electrochemical performance of the interlayer cell, which exhibits more stable cell resistance and longer cycle life relative to the all-solid-state cell.

From these results, we conclude that the modification of the electrode/electrolyte interface is of paramount importance in the development of all-solid-state lithium batteries to suppress both the electrochemical decomposition and mechanical failure of the SE. Further we show that the application of a mechanically pliable liquid interlayer is sufficient to thermodynamically protect LGPS solid electrolytes from reductive decomposition, thereby mitigating interface driven mechanical failure which would otherwise fracture the SE pellet. From this we propose that the utilization of mechanically pliable interface modifications is necessary to address many of the

mechanical instabilities resulting from interfacial decomposition reactions at the electrode/electrolyte interface during cycling.

4. Experimental Section

Electrolyte Formulation and Cell Fabrication: Unless otherwise stated, all chemicals were used as received without further purification and all sample manipulations were carried out in an Ar-filled glovebox with O₂ and H₂O concentrations <2 ppm. Electrochemical and x-ray measurements were carried out on cylindrical solid-electrolyte pellets fabricated from commercial Li₁₀GeP₂S₁₂ powder (LGPS, 99.99%, MSE Supplies LLC). Pellets were assembled by first grinding the as-received LGPS powder in a mortar and pestle to break up large aggregates. This powder was then cold pressed under static load (1500 PSI, 3 min) in a stainless-steel pellet die (International Crystal Laboratories) to a diameter of ca. 2 mm and a thickness of ca. 150 μm. Pressed pellets were stored under an Ar atmosphere until use. The solvated liquid electrolyte used for interlayer cells was prepared as described previously.^[30] Briefly, lithium bis(trifluoromethanesulfonyl)imide (LiTFSI, 99.95% Sigma-Aldrich) was dissolved in 50:50 wt.% 1, 3-dioxolane (DOL, anhydrous, Sigma-Aldrich): 1, 2-dimethoxyethane (DME, anhydrous, 99.5%, Sigma-Aldrich) in a ratio of 7 mols of LiTFSI per liter of solvent. This neat electrolyte was then diluted with one part 1,1,2,2-tetrafluoroethyl 2,2,3,3-tetrafluoropropyl ether (TTE, 99%, Synquest Laboratories) to five parts neat solvate by volume to reduce viscosity and improve ionic conductivity.^[30, 59]

Lithium symmetric cells were used to evaluate mechanical changes to the solid-electrolyte pellets during electrochemical cycling both in the presence and absence of a solvate interlayer. To maintain adequate x-ray transmission for tomographic reconstructions, electrode stacks were assembled in custom nylon Swagelok cells. LGPS cells assembled without an interlayer were constructed from bottom to top as follow: lithium metal was mechanically polished and affixed to

a 3 mm-diameter stainless-steel post to serve as the counter/reference electrode. This electrode was then inserted into the nylon cell body followed by an LGPS pellet and the working electrode, which consisted of polished lithium pressed onto a stainless-steel "I"-piece. To complete the assembly a spring was added to maintain stack pressure followed by another steel post to maintain electrical contact (detailed schematic depictions of both the electrochemical cell and the electrode stack are presented in the SI, Figure S1). Interlayer cells were fabricated in the same order with one modification in that a small amount ($<1 \mu\text{L}$) of solvate was added to the surface of each lithium electrode prior to contacting the LGPS pellet.

X-Ray Measurements: X-ray tomography was conducted at the 7-BM beamline at the Advanced Photon Source at Argonne National Laboratory. Fully assembled electrochemical cells were transported to the beamline under an Ar atmosphere and mounted on a rotating stage in the path of the x-ray beam. To mitigate potential atmospheric exposure, cells were housed in a cylindrical acrylic enclosure and purged continuously with Ar gas for the duration of the experiment. Transmission x-ray images were collected using monochromatic x-rays ($30.25 \pm 1 \text{ keV}$), which illuminated a $100 \mu\text{m}$ LuAG:Ce scintillator, followed by a visible light turning mirror. A visible light camera (FLIR Grasshopper3) equipped with a 5x long-distance microscope collected the images. The system afforded an effective pixel resolution of $1.172 \mu\text{m}$ horizontally and vertically. A fly scanning procedure was used for the tomography rotation to minimize the radiation dose on the cell.

Typical *operando* measurements consisted of a short (ca. 1000 s) open circuit potential hold followed by voltammetric cycling at a scan rate of $200 \mu\text{V s}^{-1}$ between $\pm 100 \text{ mV}$ vs Li/Li^+ to verify nominal cell performance. After ensuring normal cell function, the potential window was expanded to $\pm 500 \text{ mV}$ vs Li/Li^+ (still scanning at $200 \mu\text{V s}^{-1}$) and the cell was cycled until failure (defined as a total cell short). In tandem with electrochemical measurements, tomographic data

was collected every 500 seconds during which time the cell was rotated 360 degrees around its z-axis to provide a complete view of the interior cell volume. Prior to each scan, images were collected both with the cell removed from the camera field of view and with the x-ray beam off to produce a series of brightfield and darkfield images respectively.

Tomographic Reconstruction and Data Processing: Raw tomographic data was processed using the open source Python utility TomoPy to generate x-ray attenuation data across the cell volume, as described elsewhere.^[60] Briefly, the reconstructions used a fast Fourier transform from the projection domain into the volume domain to determine the pixel intensity at each point within the sample volume. Brightfield and darkfield images were used to normalize the projection data. Additional image corrections were undertaken in the form of a post-processing algorithm to remove obvious artifacts left by the reconstruction, primarily ring artifacts (an example of which is provided in the SI, Figure S5). Ring removal relied again on Fourier and wavelet image transforms to remove aberrations exhibiting periodicity about the center of rotation.

Analysis and rendering of the volume data, including determination of pellet void volume, was accomplished in MATLAB (see Figure S2 of the supplemental). Wherever appropriate, computation relied on population analyses of pixel intensity to maintain statistically valid interpretations of the data and to avoid erroneous pixel counting. A detailed description of the computational methods employed is provided in the SI.

Acknowledgements

This work was supported as part of the Center for Electrochemical Energy Science, an Energy Frontier Research Center funded by the U.S. Department of Energy, Office of Science, Basic Energy Science. Work was carried out in part in the Materials Research Laboratory Central Research Facilities, University of Illinois. Tomographic measurements used resources of the 7-BM beamline of the Advanced Photon Source, a U.S. Department of Energy (DOE) Office of

Science User Facility operated for the DOE Office of Science by Argonne National Laboratory under Contract No. DE-AC02-06CH11357. K.L.B. acknowledges support from the National Science Foundation Graduate Research Fellowship Program under Grant No. DGE-1144245.

Conflict of Interest

The authors declare no conflict of interest

Supporting Information

Supporting Information is available from the Wiley Online Library or from the author.

References

- [1] J. B. Goodenough, K. S. Park, *J Am Chem Soc* **2013**, *135* (4), 1167.
- [2] A. Manthiram, *ACS Central Sci* **2017**, *3* (10), 1063.
- [3] X. B. Cheng, R. Zhang, C. Z. Zhao, Q. Zhang, *Chem. Rev.* **2017**, *1117* (15), 10403.
- [4] K. Xu, *Chem Rev* **2004**, *104* (10), 4303.
- [5] X. N. Feng, M. G. Ouyang, X. Liu, L. G. Lu, Y. Xia, X. M. He, *Energy Storage Mater* **2018**, *10*, 246.
- [6] N. E. Galushkin, N. N. Yazvinskaya, D. N. Galushkin, *J Electrochem Soc* **2018**, *165* (7), A1303.
- [7] F. Zheng, M. Kotobuki, S. F. Song, M. O. Lai, L. Lu, *J Power Sources* **2018**, *389*, 198.
- [8] L. Frenck, G. K. Sethi, J. A. Maslyn, N. P. Balsara, *Front Energy Res* **2019**, *7*, 115.
- [9] T. Inoue, K. Mukai, *ACS. Appl. Mater. Interfaces* **2017**, *9* (2), 1507.
- [10] S. Xia, X. Wu, Z. Zhang, Y. Cui, W. Liu, *Chem* **2019**, *5*, 753.
- [11] S. J. Chen, D. J. Xie, G. Z. Liu, J. P. Mwizerwa, Q. Zhang, Y. R. Zhao, X. X. Xu, X. Y. Yao, *Energy Storage Mater* **2018**, *14*, 58.
- [12] N. Kamaya, K. Homma, Y. Yamakawa, M. Hirayama, R. Kanno, M. Yonemura, T. Kamiyama, Y. Kato, S. Hama, K. Kawamoto, A. Mitsui, *Nat Mater* **2011**, *10* (9), 682.
- [13] G. F. Dewald, S. Ohno, M. A. Kraft, R. Koerver, P. Till, N. M. Vargas-Barbosa, J. Janek, W. G. Zeier, *Chem Mater* **2019**, *31* (20), 8328.
- [14] F. D. Han, Y. Z. Zhu, X. F. He, Y. F. Mo, C. S. Wang, *Adv Energy Mater* **2016**, *6* (8), 1501590.
- [15] W. D. Richards, L. J. Miara, Y. Wang, J. C. Kim, G. Ceder, *Chem Mater* **2016**, *28* (1), 266.

- [16] S. A. Peryez, M. A. Cambaz, V. Thangadurai, M. Fichtnert, *ACS Appl Mater Inter* **2019**, *11* (25), 22029.
- [17] K. H. Nie, Y. S. Hong, J. L. Qiu, Q. H. Li, X. Q. Yu, H. Li, L. Q. Chen, *Front Chem* **2018**, *6*, 616.
- [18] Y. H. Xiao, Y. Wang, S. H. Bo, J. C. Kim, L. J. Miara, G. Ceder, *Nat Rev Mater* **2020**, *5* (2), 105.
- [19] L. Z. Sang, R. T. Haasch, A. A. Gewirth, R. G. Nuzzo, *Chem Mater* **2017**, *29* (7), 3029.
- [20] S. Wenzel, S. Randau, T. Leichtweiss, D. A. Weber, J. Sann, W. G. Zeier, J. Janek, *Chem Mater* **2016**, *28* (7), 2400.
- [21] F. Y. Shen, M. B. Dixit, X. H. Xiao, K. B. Hatzell, *ACS Energy Lett* **2018**, *3* (4), 1056.
- [22] F. Sun, K. Dong, M. Osenberg, A. Hilger, S. Risse, Y. Lu, P. H. Kamm, M. Klaus, H. Markotter, F. Garcia-Moreno, T. Arlt, I. Manke, *J Mater Chem A* **2018**, *6* (45), 22489.
- [23] J. Tippens, J. C. Miers, A. Afshar, J. A. Lewis, F. J. Q. Cortes, H. P. Qiao, T. S. Marchese, C. V. Di Leo, C. Saldana, M. T. McDowell, *ACS Energy Lett* **2019**, *4* (6), 1475.
- [24] N. Seitzman, H. Guthrey, D. B. Sulas, H. A. S. Platt, M. Al-Jassim, S. Pylypenko, *J Electrochem Soc* **2018**, *165* (16), A3732.
- [25] M. J. Du, K. M. Liao, Q. Lu, Z. P. Shao, *Energ Environ Sci* **2019**, *12* (6), 1780.
- [26] A. Gurung, J. Pokharel, A. Baniya, R. Pathak, K. Chen, B. S. Lamsal, N. Ghimire, W. H. Zhang, Y. Zhou, Q. Q. Qiao, *Sustain Energ Fuels* **2019**, *3* (12), 3279.
- [27] D. Bosubahu, J. Sivaraj, R. Sampathkumar, K. Ramesha, *ACS Appl Energ Mater* **2019**, *2* (6), 4118.
- [28] F. J. Simon, M. Hanauer, F. H. Richter, J. Janek, *ACS Appl Mater Interfaces* **2020**, *12* (10), 11713.

- [29] Q. Liu, Q. P. Yu, S. Li, S. W. Wang, L. H. Zhang, B. Y. Cai, D. Zhou, B. H. Li, *Energy Storage Mater* **2020**, *25*, 613.
- [30] M. A. Philip, P. T. Sullivan, R. X. Zhang, G. A. Wooley, S. A. Kohn, A. A. Gewirth, *ACS Appl Mater Inter* **2019**, *11* (2), 2014.
- [31] Y. Wu, N. Liu, *Chem* **2018**, *4*, 438
- [32] L. Z. Sang, K. L. Bassett, F. C. Castro, M. J. Young, L. Chen, R. T. Haasch, J. W. Elam, V. P. Dravid, R. G. Nuzzo, A. A. Gewirth, *Chem Mater* **2018**, *30* (24), 8747.
- [33] A. J. Bard, L. R. Faulkner, *Electrochemical Methods. 2nd ed.*, John Wiley & Sons, Inc., Hoboken, NJ, USA, **2001**.
- [34] Y. Z. Zhu, X. F. He, Y. F. Mo, *J Mater Chem A* **2016**, *4* (9), 3253.
- [35] S. Wenzel, D. A. Weber, T. Leichtweiss, M. R. Busche, J. Sann, J. Janek, *Solid State Ionics* **2016**, *286*, 24.
- [36] M. Shin, A. A. Gewirth, *Adv Energy Mater* **2019**, *9* (26), 1900938.
- [37] X. Judez, M. Martinez-Ibanez, A. Santiago, M. Armand, H. Zhang, C. M. Li, *J Power Sources* **2019**, 438.
- [38] P. Bonnick, K. Niitani, M. Nose, K. Suto, T. S. Arthur, J. Muldoon, *J Mater Chem A* **2019**, *7* (42), 24173.
- [39] S. Yang, W. W. Wang, C. Lin, W. X. Shen, Y. D. Li, *Energies* **2019**, *12* (10), 1885.
- [40] Y. Suzuki, D. S. Cousins, J. R. Dorgan, A. P. Stebner, B. B. Kappes, *J Compos Mater* **2019**, *53* (17), 2349.
- [41] P. Pietsch, V. Wood, *Annu Rev Mater Res* **2017**, *47*, 451.
- [42] J. Lai, G. W. Wang, Z. Y. Fan, J. Chen, Z. Q. Qin, C. W. Xiao, S. C. Wang, X. Q. Fan, *Sci Rep* **2017**, *7*, 1825.

- [43] L. Xu, S. Tang, Y. Cheng, K. Y. Wang, J. Y. Liang, C. Liu, Y. C. Cao, F. Wei, L. Q. Mai, *Joule* **2018**, 2 (10), 1991.
- [44] X. Zhang, Q. J. Wang, K. L. Harrison, S. A. Roberts, S. J. Harris, *Cell Reports Physical Science* **2020**, 1, 100012
- [45] M. J. Berger, J. H. Hubbell, S. M. Seltzer, J. Chang, J. S. Coursey, R. Sukumar, D. S. Zucker, K. Olsen, XCOM: Photon Cross Section Database (version 1.5), <http://physics.nist.gov/xcom>, accessed: 03, 2020.
- [46] G. V. Samsonov, *Handbook of the Physicochemical Properties of the Elements*. Springer, Boston, MA, USA, **1968**.
- [47] J. Park, S. H. Yu, Y. E. Sung, *Nano Today* **2018**, 18, 35.
- [48] N. Auner, U. Klingebiel, in *Synthetic Methods of Organometallic and Inorganic Chemistry*, Vol. 2, (Eds. W. A. Hermann), Thieme, Stuttgart, New York, **1996**.
- [49] J. Weker Nelson, N. Liu, J. C. Andrews, Y. Cui, M. F. Toney, *Energy Environ. Sci.* **2013**, 7, 2771.
- [50] H. Liu, X. B. Cheng, J. Q. Huang, H. Yuan, Y. Lu, C. Yan, G. L. Zhu, R. Xu, C. Z. Zhao, L. P. Hou, C. He, S. Kaskel, Q. Zhang, *ACS Energy Lett* **2020**, 5, 833.
- [51] D. A. Weber, A. Senyshyn, K. S. Weldert, S. Wenzel, W. B. Zhang, R. Kaiser, S. Berendts, J. Janek, W. G. Zeier, *Chem Mater* **2016**, 28 (16), 5905.
- [52] Z. Q. Wang, M. S. Wu, G. Liu, X. L. Lei, B. Xu, C. Y. Ouyang, *Int J Electrochem Sc* **2014**, 9 (2), 562.
- [53] C. Monroe, J. Newman, *J Electrochem Soc* **2005**, 152 (2), A396.
- [54] S. Yu, R. D. Schmidt, R. Garcia-Mendez, E. Herbert, N. J. Dudney, J. B. Wolfenstine, J. Sakamoto, D. J. Siegel, *Chemistry of Materials* **2016**, 28 (1), 197.
- [55] A. Sakuda, A. Hayashi, M. Tatsumisago, *Sci Rep* **2013**, 3, 2261.

- [56] A. Ferrese, P. Albertus, J. Christensen, J. Newman, *J. Electrochem. Soc.* **2012**, 159, A1615.
- [57] A. Ferrese, J. Newman, *J. Electrochem. Soc.* **2014**, 161, A948.
- [58] A. Ferrese, J. Newman, *J. Electrochem. Soc.* **2014**, 161, A1350.
- [59] M. J. Shin, H. L. Wu, B. Narayanan, K. A. See, R. S. Assary, L. Y. Zhu, R. T. Haasch, S. Zhang, Z. C. Zhang, L. A. Curtiss, A. A. Gewirth, *ACS Appl Mater Inter* **2017**, 9 (45), 39357.
- [60] D. Gursoy, F. De Carlo, X. H. Xiao, C. Jacobsen, *J Synchrotron Radiat* **2014**, 21, 1188.

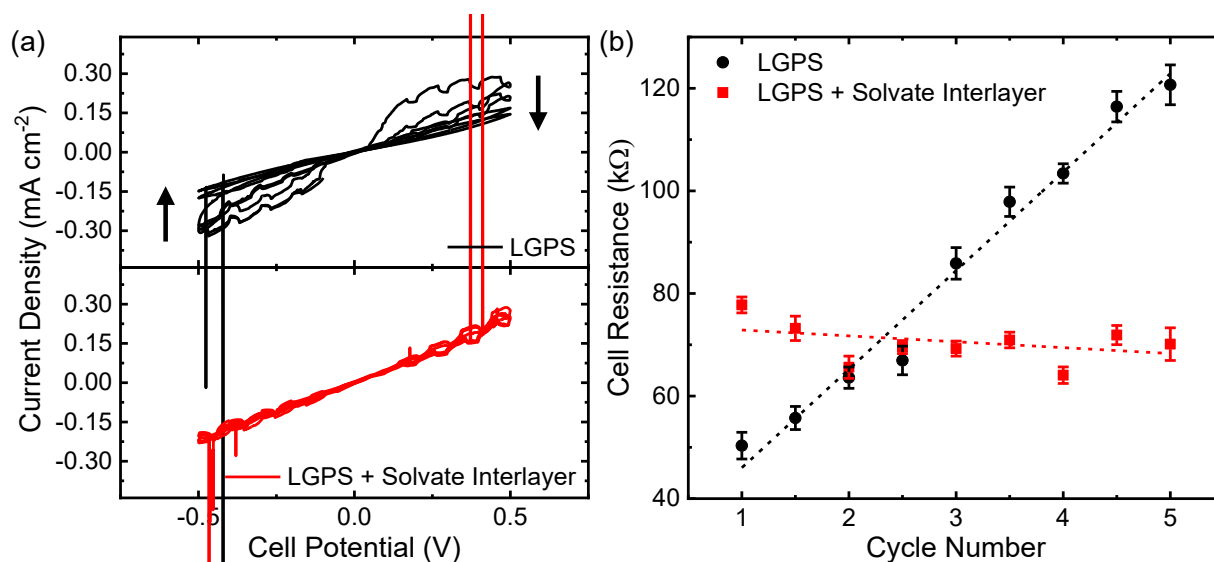


Figure 1. (a) Cyclic voltammograms of an all-solid-state LGPS cell (black) and an LGPS cell with solvate interlayers applied to the surfaces of each lithium electrode (red). (b) Cell resistance for each potential sweep for both the all-solid-state (black) and interlayer cell (red) plotted as a function of cycle number.

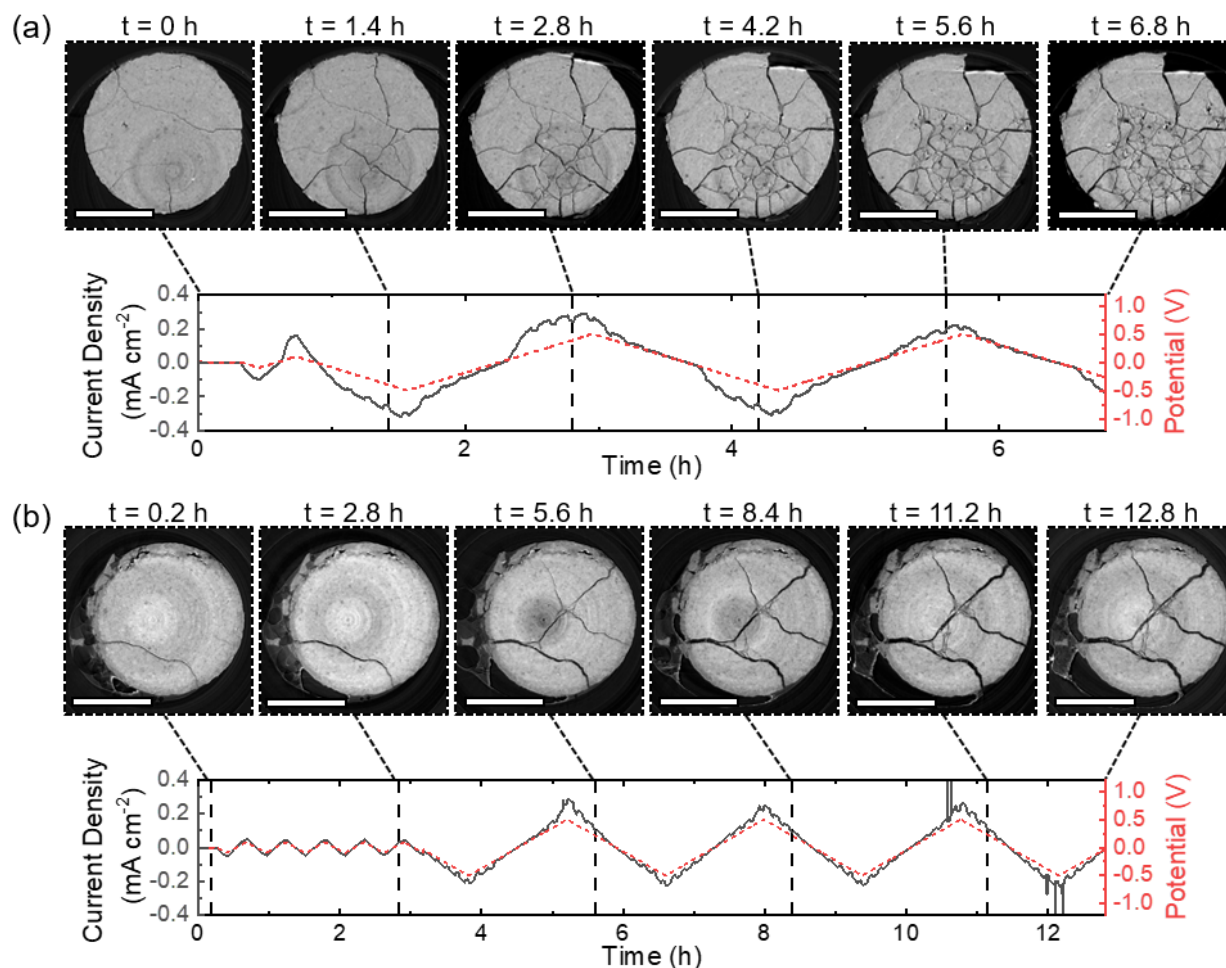


Figure 2. Cross-sectional images of an (a) all-solid-state and (b) interlayer cell during voltammetric cycling plotted as a function of time along with the cell voltage (dashed red traces) and cell current (black traces) for each cell. Pixel brightness reflects x-ray attenuation with bright pixels representing the LGPS pellet and darkest pixels representing empty space. Images were taken at the center of each LGPS pellet with scale bars denoting 1 mm.

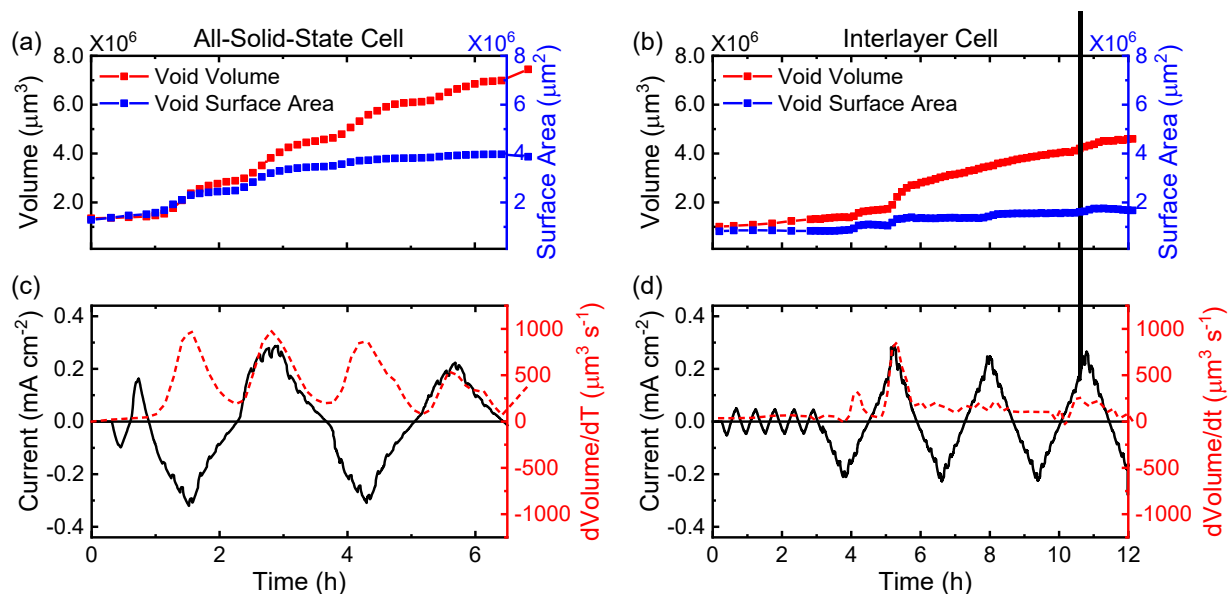


Figure 3. Computed void volumes (red) and void surface areas (blue) of solid electrolyte pellets during voltammetric cycling in the (a) absence and (b) presence of a solvate interlayer. (c) and (d) depict the derivative void volumes (dashed red traces) plotted as a function of time for the all-solid-state and interlayer cells, respectively, along with the currents (solid black traces) elicited by these cells during cycling.

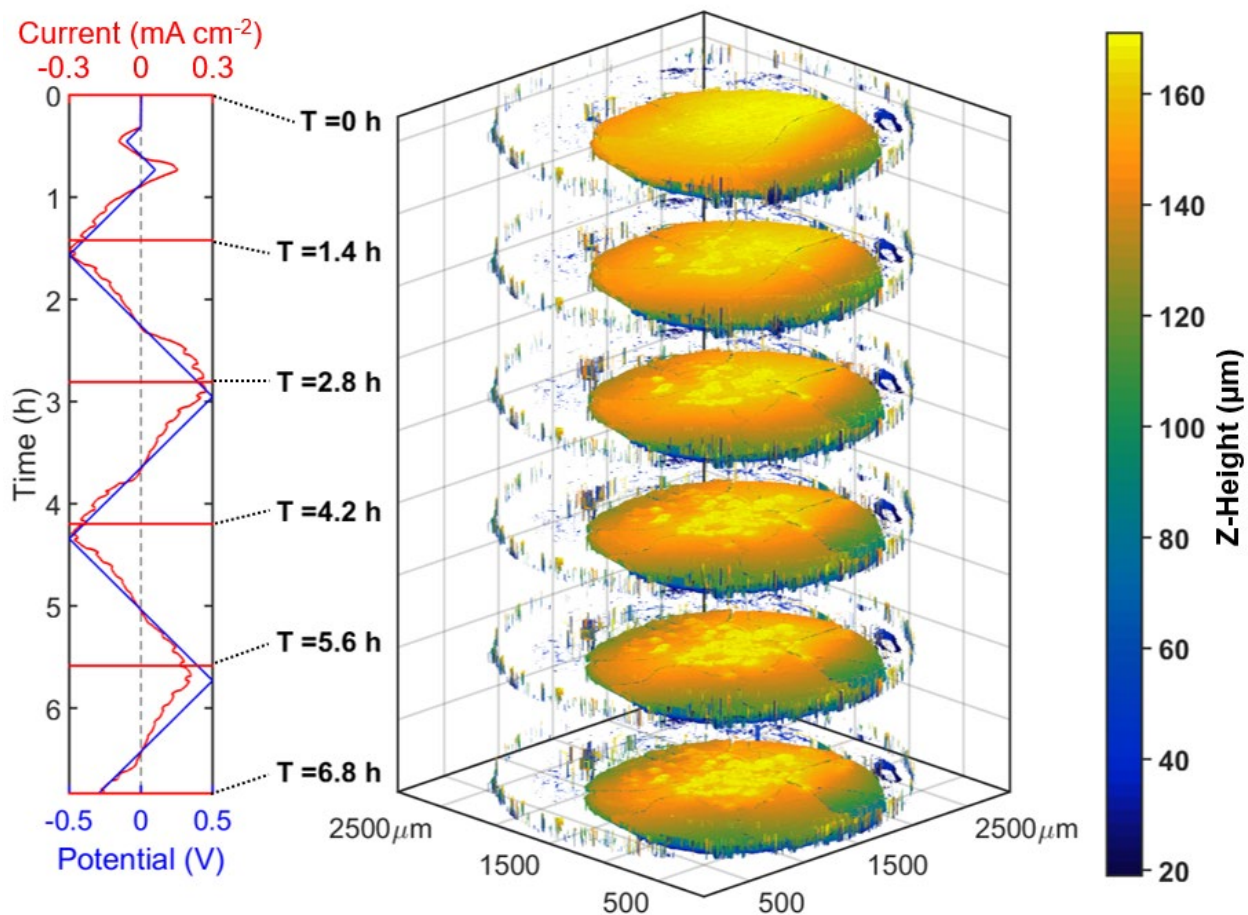


Figure 4. Electrochemical cycling and accompanying three dimensional renderings of an LGPS pellet in the all-solid-state configuration. As cycling progresses a substantial morphological change is observed at the pellet surface as evidenced by the increased roughness and accumulation of high elevation (bright yellow) domains.

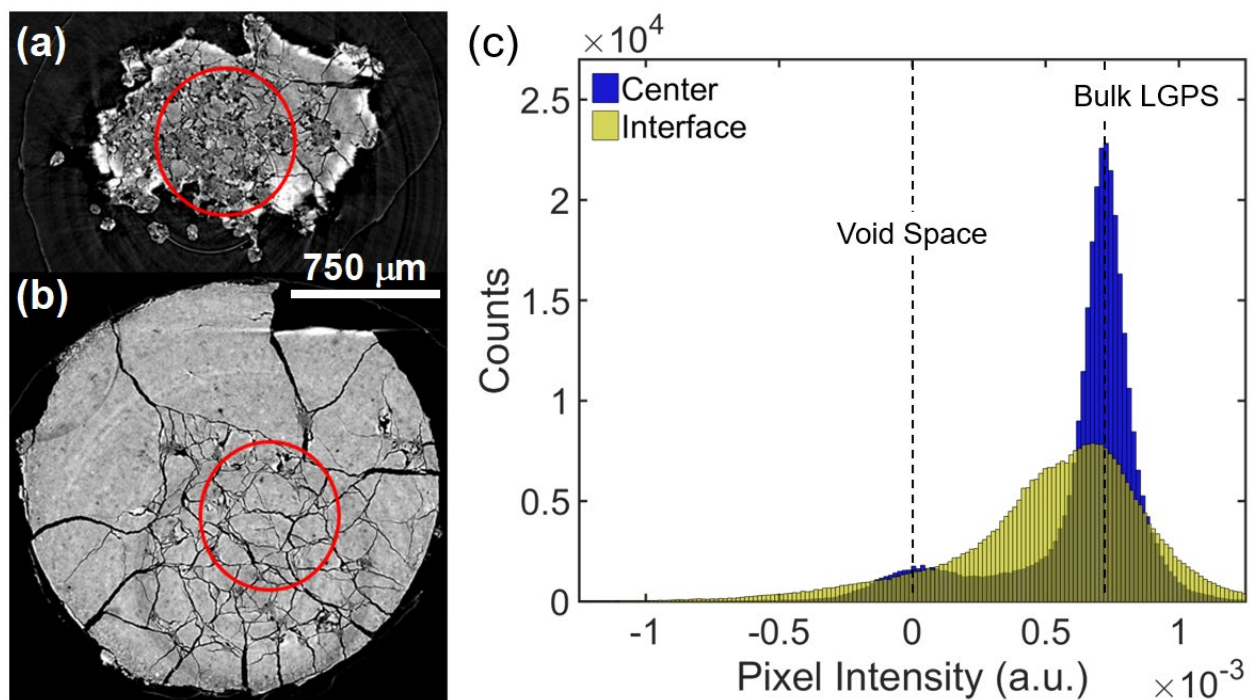


Figure 5. Reconstructed tomographic images collected from an all-solid-state cell (a) near the LGPS/Li⁰ interface and (b) at the center of the LGPS pellet at the end of cycling ($t \approx 6.8$ h). (c) Presents a histogram analysis of pixel intensities collected from images a and b demonstrating a large population of pixels with intermediate intensity near the LGPS/Li interface that cannot be attributed to either bulk LGPS or void space/Li.

Table 1. Parameters used and results obtained from a pixel intensity analysis near the LGPS/Li⁰ interface for an all-solid-state LGPS cell. The table includes the density ρ , x-ray mass attenuation coefficient μ/ρ , total attenuation coefficient μ , experimental pixel intensity if known, and estimated pixel intensity for each species under consideration.

| Species | ρ (g cm ⁻³) | μ/ρ (cm ² g ⁻¹) | μ (cm ⁻¹) | Pixel Intensity (Experimental) ^{a)} | Pixel Intensity (Calculated) |
|--|--|--|------------------------------|---|---------------------------------|
| Li ₁₀ GeP ₂ S ₁₂ pellet | 1.5 ± 0.1 | 3.29 | 4.9 ± 0.3 | 6.4 ± 0.7 × 10 ⁻⁴ | - |
| Li ⁰ | 0.53 ^[46] | 0.16 | 8.8 × 10 ⁻² | 0.0 ± 0.3 × 10 ⁻⁴ | - |
| Ar (void space) | 1.7 × 10 ⁻³ ^[46] | 2.7 | 4.6 × 10 ⁻³ | 0.0 ± 0.4 × 10 ⁻⁴ | - |
| Interfacial species | - | - | - | 4.5 ± 1.0 × 10 ⁻⁴ | - |
| Li ₂ S | 1.66 ^[47] | 1.5 | 2.53 | - | 3.3 ± 0.4 × 10 ⁻⁴ |
| Li ₃ P | 1.43 ^[48] | 1.1 | 1.55 | - | 2.0 ± 0.2 × 10 ⁻⁴ |
| Li _{3.75} Ge | 1.76 ^[49] | 10.2 | 17.8 | - | 23.1 ± 2.5 × 10 ⁻⁴ |
| 12 Li ₂ S + 2 Li ₃ P + Li _{3.75} Ge | - | - | 3.42 | - | 4.4 ± 0.5 × 10 ⁻⁴ |

^{a)} Uncertainties were determined from the standard deviation in the pixel distribution of the LGPS pellet and were propagated to the calculated pixel intensities.

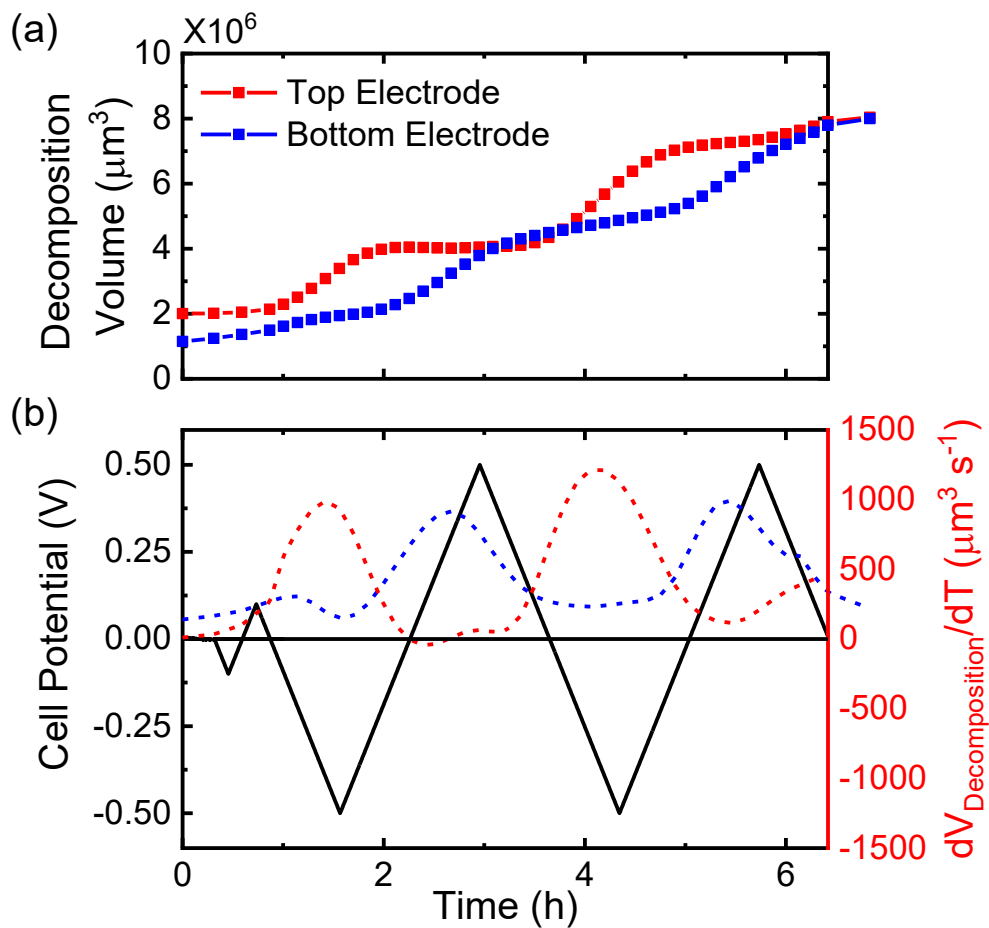


Figure 6. (a) Computed volumes of decomposed material formed at the top (red) and bottom (blue) electrode/LGPS interfaces. (b) Derivative traces of the decomposition volume at the top (red dashed trace) and bottom (blue dashed trace) electrodes plotted against time along with the accompanying cell voltage profile (solid black trace).

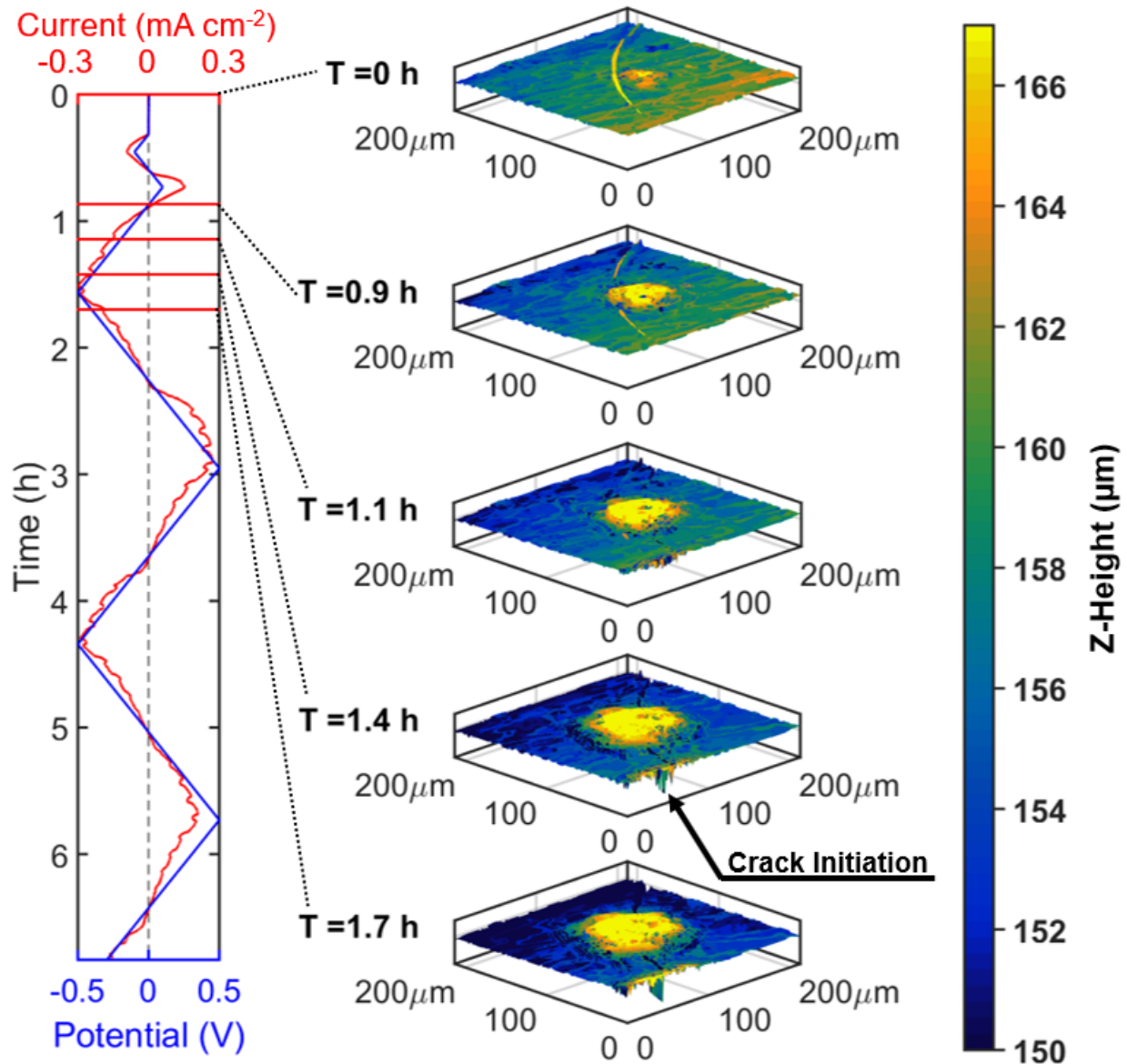


Figure 7. Three-dimensional renderings of a single decomposition domain while polarizing the top electrode reductively. As the potential is reduced the size of the inclusion increases radially and vertically. After a certain point ($t = 1.4 \text{ h}$) the inclusion exerts sufficient pressure on the LGPS sub-structure and a crack forms at the locus of the inclusion.

Table 2. Computed critical volumes of material inclusions and critical stress (σ_c) developed at the point of pellet fracture.

| Inclusion Height (μm) | Inclusion Radius (μm) | Inclusion Volume (μm^3) | E_{LGPS} (GPa) ^[51] | E_{Li} (GPa) ^[46] | σ_c (GPa) |
|------------------------------------|------------------------------------|--------------------------------------|---|---------------------------------------|------------------|
| 19 ± 3 | 72 ± 20 | $1.7 \pm 0.3 \times 10^5$ | 10.5 | 4.9 | 0.8 ± 0.2 |

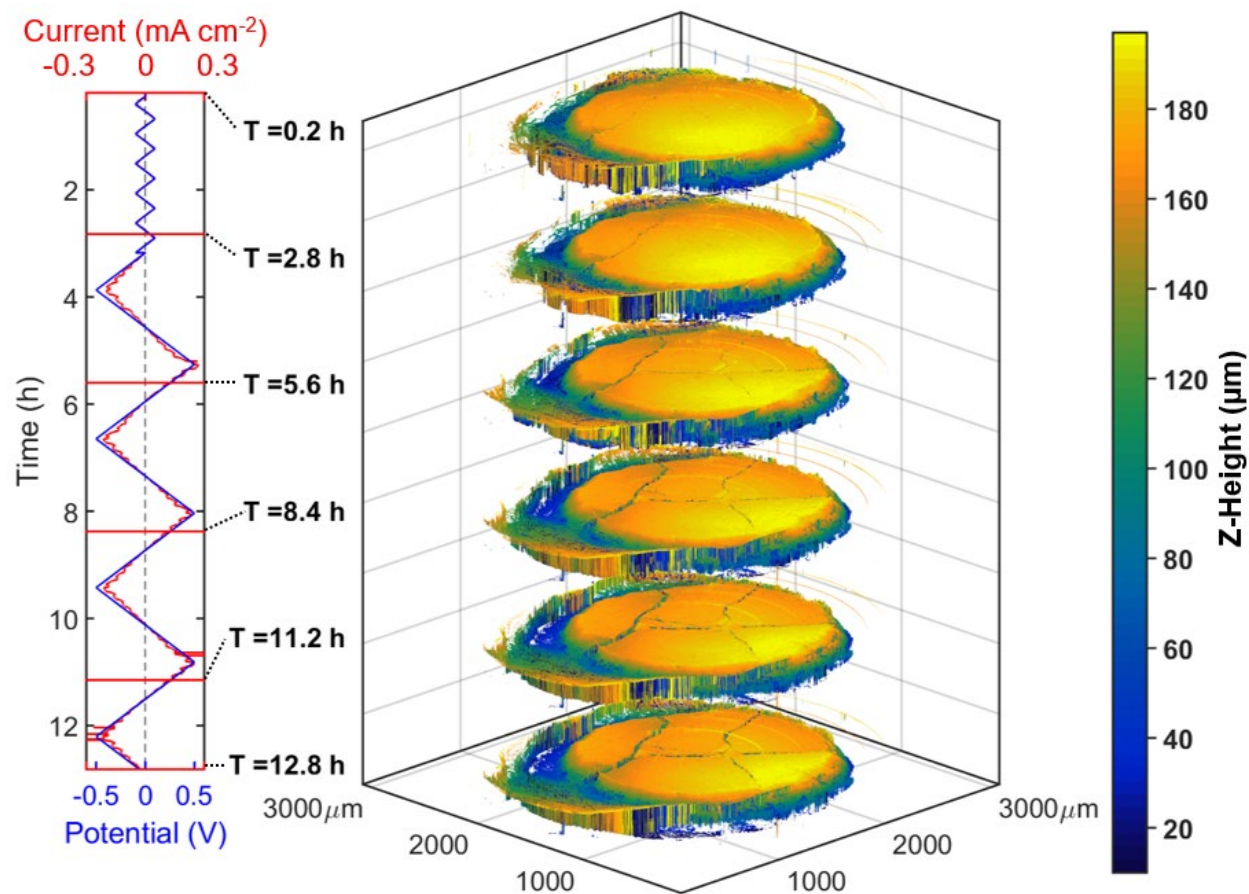


Figure 8. Three-dimensional renderings of an LGPS cell with solvate interlayers applied to both sides of the SE pellet. Crack formation is evident as cycling progresses, however in contrast to the all-solid-state-cell no obvious morphological changes are observed at the pellet surface during cell cycling

ToC Entry:

Herein, the interfacial mechanical properties of the solid electrolyte (SE) $\text{Li}_{10}\text{GeP}_2\text{S}_{12}$ are interrogated with *Operando* x-ray tomography. The origin of mechanical failure in SE pellets is revealed to be the electrochemical decomposition of the SE at the electrode/electrolyte interface. Further, the electrochemical and mechanical instabilities can be suppressed by the application of a liquid interlayer to the interface.

Keywords:

(Solid Electrolyte, X-Ray Tomography, Mechanical Failure, LGPS, Solvate)

Authors:

*Kenneth E. Madsen, Kimberly L. Bassett, Kim Ta, Brandon A. Sforzo, Katarzyna E. Matusik¹, Alan L. Kastengren, and Andrew A. Gewirth**

Title:

Direct Observation of Interfacial Mechanical Failure in Thio-Phosphate Solid Electrolytes

with *Operando* X-Ray Tomography

